

See discussions, stats, and author profiles for this publication at: <https://www.researchgate.net/publication/235399488>

A Highly Efficient $\text{TiO}_2\text{-xCx}$ Nano-heterojunction Photocatalyst for Visible Light Induced Antibacterial Applications

ARTICLE in ACS APPLIED MATERIALS & INTERFACES · FEBRUARY 2013

Impact Factor: 6.72 · DOI: 10.1021/am302676a · Source: PubMed

CITATIONS

48

READS

76

5 AUTHORS, INCLUDING:



Vinodkumar Etacheri

Purdue University

23 PUBLICATIONS 1,571 CITATIONS

SEE PROFILE



Michael Seery

Dublin Institute of Technology

29 PUBLICATIONS 1,708 CITATIONS

SEE PROFILE



Steven J. Hinder

University of Surrey

61 PUBLICATIONS 1,241 CITATIONS

SEE PROFILE



Suresh C Pillai

IT Sligo

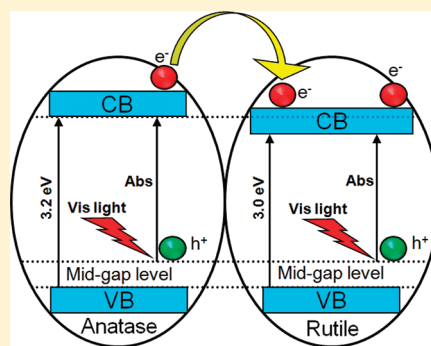
65 PUBLICATIONS 2,512 CITATIONS

SEE PROFILE

Nanostructured $\text{Ti}_{1-x}\text{S}_x\text{O}_{2-y}\text{N}_y$ Heterojunctions for Efficient Visible-Light-Induced PhotocatalysisVinodkumar Etacheri,^{†,‡} Michael K. Seery,[‡] Steven J. Hinder,[§] and Suresh C. Pillai^{*,†}[†]Centre for Research in Engineering Surface Technology (CREST), FOCAS Institute, and [‡]School of Chemical and Pharmaceutical Sciences, Dublin Institute of Technology, Kevin Street, Dublin 8, Ireland[§]The Surface Analysis Laboratory, Faculty of Engineering and Physical Sciences, University of Surrey, Guildford, Surrey, GU2 7XH, United Kingdom

S Supporting Information

ABSTRACT: Highly visible-light-active S,N-codoped anatase–rutile heterojunctions are reported for the first time. The formation of heterojunctions at a relatively low temperature and visible-light activity are achieved through thiourea modification of the peroxy–titania complex. FT-IR spectroscopic studies indicated the formation of a Ti^{4+} –thiourea complex upon reaction between peroxy–titania complex and thiourea. Decomposition of the Ti^{4+} –thiourea complex and formation of visible-light-active S,N-codoped TiO_2 heterojunctions are confirmed using X-ray diffraction, Raman spectroscopy, transmission electron microscopy, and UV/vis spectroscopic studies. Existence of sulfur as sulfate ions (S^{6+}) and nitrogen as lattice (N–Ti–N) and interstitial (Ti–N–O) species in heterojunctions are identified using X-ray photoelectron spectroscopy (XPS) and FT-IR spectroscopic techniques. UV–vis and valence band XPS studies of these S,N-codoped heterojunctions proved the fact that the formation of isolated S 3p, N 2p, and Π^* N–O states between the valence and conduction bands are responsible for the visible-light absorption. Titanium dioxide obtained from the peroxy–titania complex exists as pure anatase up to a calcination temperature as high as 900 °C. Whereas, thiourea-modified samples are converted to S,N-codoped anatase–rutile heterojunctions at a temperature as low as 500 °C. The most active S,N-codoped heterojunction 0.2 TU- TiO_2 calcined at 600 °C exhibits a 2-fold and 8-fold increase in visible-light photocatalytic activities in contrast to the control sample and the commercial photocatalyst Degussa P-25, respectively. It is proposed that the efficient electron–hole separation due to anatase to rutile electron transfer is responsible for the superior visible-light-induced photocatalytic activities of S,N-codoped heterojunctions.



1. INTRODUCTION

Significant advances have recently been made in the applications of titania nanomaterials for photocatalysis, organic synthesis, solar cells, water and air purification, self-cleaning antibacterial materials, cancer therapy, and cathodic corrosion protection.^{1–13} High redox potential, chemical stability, inexpensiveness, and nontoxicity were identified as the main reasons responsible for the wide acceptability of titania materials in contrast to other semiconductor photocatalysts.^{2–4}

Several factors such as phase purity, surface area, crystallite size, amount and nature of dopants, method of preparation, and anatase–rutile ratio strongly affect the efficiency of titania photocatalysts.^{14,15} Anatase phase titania was found to be a better photocatalyst in comparison to the rutile or brookite polymorphs due to its higher charge-carrier mobility and an increased density of surface hydroxyls.^{16–18}

However, the visible-light photocatalytic applications of the anatase phase was restricted due to its wide band gap (3.2 eV), which makes it active only under UV light ($\lambda \leq 387.5$ nm) irradiation. The rutile phase titania with a smaller band gap of 3.0 eV was also found to be less visible-light-active due to the lower redox potential of electron–hole pairs generated and

their faster recombination rate.¹⁹ In order to efficiently exploit the sunlight or light from artificial sources, the development of a highly visible-light-active photocatalyst is necessary. A variety of methods for visible-light activation such as metal and nonmetal doping, dye sensitization, and optimization of phase composition have been investigated previously.^{20–22} In addition to this, we have recently reported the synthesis of visible-light-active oxygen-rich titania nanoparticles.² After the report of nitrogen and other anion (S, C, and F) doped titania by Asahi and co-workers, titania doped with main group elements has attracted a great deal of interest.²⁰ Among the various anion-doped titania reported, sulfur (S) and nitrogen (N) doped titania photocatalysts were found to have better visible-light photocatalytic activities.^{3,4,21} Due to the higher ionic radius of S^{2-} in contrast to N^{3-} , S-doping can significantly modify the electronic structure of titania and absorb more visible-light.²² Depending on the synthetic method, sulfur was detected in the form of sulfide (S^{2-}), hexavalent (S^{6+}), or tetravalent (S^{4+}) in titania.^{23–27} The cationic S-doped titania reported by Ohno et

Received: January 22, 2012

Published: June 12, 2012



al. were found to have better visible-light absorption and photocatalytic activities in comparison to the anionic S-doped titania.²⁴ Periyat et al. recently reported the coexistence of cationic sulfur and anionic nitrogen in titanium dioxide photocatalysts.²¹ In addition to this, S,N-codoped titania recently reported by many researchers was found to have better photocatalytic activities over titania containing either S or N alone.^{28–30}

The major drawback of anion-doped titania is the increased electron–hole recombination due to the impurity energy levels formed in the band gap.^{31,32} In order to overcome this problem, coupling of S,N-codoped titania with the electron–hole separating agents such as metal nanoparticles or small band gap semiconductors such as rutile is necessary.^{3,31,33} Improved photocatalytic activities of anatase–rutile mixtures in comparison to pure anatase or rutile alone were also reported previously.^{4,14,34} For example, Degussa P-25, which is a mixture of approximately 70% anatase and 30% rutile, exhibited greater photocatalytic activities in contrast to other single-phase titania photocatalysts. Effective electron transfer from anatase to rutile was found to be responsible for the enhanced activities of these biphasic photocatalysts. Moreover, we have recently reported the enhanced visible-light photocatalytic activities of N-doped anatase–rutile nanoheterojunctions.³ Under normal synthetic conditions, anatase–rutile mixtures can only be obtained above 700 °C, which usually results in excessive crystallite growth and poor photocatalytic activities.⁴ Most of the low-temperature methods for the synthesis of S,N-codoped titania result only in the formation of anatase phase titania.^{29,35} In addition to this, sulfur, nitrogen, and their codoping were reported to be stabilizing anatase phase at higher temperatures (>800 °C).^{4,21} To the best of our knowledge, there are no systematic studies reported for the synthesis of S,N-codoped anatase–rutile heterojunctions. For the first time, this has been achieved through a thiourea-modified peroxo–titania route. Simultaneous low-temperature crystallization of rutile phase and the visible-light activation was attained through S,N-codoping by employing thiourea as a precursor modifier. The mechanism of S,N-codoped heterojunction ($\text{Ti}_{1-x}\text{S}_x\text{O}_{2-y}\text{N}_y$) formation, the effect of thiourea concentration on the phase formation, and factors responsible for their superior visible-light photocatalytic activities were explored.

2. EXPERIMENTAL METHODS

2.1. Synthesis of $\text{Ti}_{1-x}\text{S}_x\text{O}_{2-y}\text{N}_y$ Heterojunctions. The thiourea-modified peroxo–titania route was employed for the synthesis of S,N-codoped anatase–rutile heterojunctions. All reagents were purchased from Sigma Aldrich and used without further purification. Titanium tetrachloride (99.9%) and thiourea (99%) were used as the titania precursor and chemical modifier, respectively. In a typical synthesis of 1:0.1 thiourea-modified titania (0.1 TU– TiO_2), titanium tetrachloride (5.5 mL) was added to 150 mL of cold deionized water (5 °C) to form titanium oxychloride. Hydrated titanium dioxide was precipitated from this solution by adjusting the pH to 7 using ammonium hydroxide (15 mL). The precipitate obtained was then repeatedly washed with deionized water to free chloride ions (tested with AgNO_3 solution) and stirred with 30 wt % hydrogen peroxide solution (80 mL) and deionized water (100 mL) for 1 h to form an orange-colored peroxo–titania complex. The complex thus obtained was then mixed with thiourea (0.195 g) and stirred for 30 min. The colorless transparent solution obtained was converted to gel after heating at 50 °C for 2 h, which was then dried in an air oven at 100 °C for 24 h. The xerogel thus obtained was then calcined at 500, 600, 700, and 800 °C for 2 h at a heating rate of 10 °C/min. The same experimental procedure was employed for the synthesis of 1:0.2, 1:0.4 and 1:0.8 thiourea-modified

titania samples by using 0.390, 0.78, and 1.56 g of thiourea (identified as 0.2 TU– TiO_2 , 0.4 TU– TiO_2 , and 0.8 TU– TiO_2 , respectively, after calcination). A control titania sample was also prepared by the same synthetic method without using thiourea to compare the results.

2.2. Characterization Techniques. The FT-IR spectra of xerogel dried at 100 °C and after calcination at various temperatures were recorded in the range of 4000–400 cm^{-1} using a Perkin-Elmer GX FT-IR spectrometer. For recording the spectra, samples were uniformly mixed with KBr, and transparent pellets were prepared by using a 4 mm die. X-ray diffraction patterns ($2\theta = 10^\circ\text{--}70^\circ$) were obtained from a Siemens D 500 diffractometer working with Cu-K α radiation ($\lambda = 0.15418$ nm). The amount of the rutile phase present in heterojunctions obtained at various calcination temperatures was accurately calculated using the Spurr equation (eq 1)

$$F_R = \frac{1}{1 + 0.8[I_A(101)/I_R(110)]} \quad (1)$$

where F_R is the amount of rutile in an anatase–rutile mixture, and $I_A(101)$ and $I_R(110)$ are the anatase and rutile main peak intensities, respectively. The Scherrer equation (eq 2) was employed for the precise calculation of crystallite sizes of anatase and rutile in heterojunctions

$$\Phi = \frac{K\lambda}{\beta \cos \theta} \quad (2)$$

where Φ is the crystallite size, λ is the wavelength of X-ray used, K is the shape factor, β is the full line width at the half-maximum height of the main intensity peak, and θ is the Bragg angle.

The room-temperature Raman analysis of heterojunctions prepared at various calcination temperatures was performed using a Dilor ISA Labram 1 B micro-Raman system equipped with a 514 nm Ar⁺ ion laser. X-ray photoelectron spectra were recorded using a Thermo Fisher Scientific (East Grinstead, UK) θ probe spectrometer using monochromatic Al-K α radiation (photon energy 1486.6 eV). Absorption spectra of powder samples were obtained from a Perkin-Elmer Lambda 900 UV/vis/NIR spectrometer equipped with an integrated sphere attachment, and BaSO_4 was used as reference. Photoluminescence (PL) spectra of powder samples were recorded using a Perkin-Elmer PL spectrometer (LS-55B) at an excitation wavelength of 260 nm. A JEOL JEM-2100 TEM system working at an accelerating voltage of 200 kV was used for transmission electron microscopy (TEM). The distance between the adjacent crystal planes in anatase and rutile titania was calculated from the selected area electron diffraction (SAED) pattern using eq 3

$$d = \frac{\lambda L}{R} \quad (3)$$

where d is the distance between adjacent crystal planes, λ is the wavelength of accelerated electrons used, L is the camera length, and R is the radius of the diffraction pattern. The nitrogen adsorption and desorption isotherms were collected using a Quantachrome 2000e surface area analyzer. Additional experimental details are provided in the Supporting Information.

2.3. Photocatalysis Study. The methylene blue degradation technique was employed for the visible-light photocatalytic activity evaluation of S,N-codoped titania heterojunctions.^{36,37} Polychromatic visible light was generated using a Q-Sun solar simulator and a primary blue filter with a transmission intensity of 45% at 450 nm (Supporting Information, Figure S1). Such a filter, which is opaque to 530–680 nm light (where methylene blue absorbs light), was intentionally selected to avoid the photosensitized and photolytic decomposition of methylene blue. In a typical photocatalytic degradation experiment, titania powder (0.06 g) was mixed and stirred well with an aqueous solution of methylene blue (50 mL, 1×10^{-5} M) in a glass beaker (100 mL). The suspension thus obtained was kept in the dark for 30 min and then irradiated by visible light (0.68 W/m²) with stirring. The solar simulator was connected to an air cooler and thermostat to maintain the temperature of suspension at 25 °C. After equal time intervals of 1 h, aliquots (3 mL) were withdrawn from the suspension

under visible-light irradiation and the absorption spectra were recorded using a Perkin-Elmer Lambda 900 UV/vis/NIR spectrometer. The photocatalytic rate constant (k) for visible-light-induced methylene blue degradation was calculated from eq 4

$$\ln\left(\frac{A_0}{A}\right) = kt \quad (4)$$

where A_0 is the initial absorbance of methylene blue solution, A is the absorbance after a time t , and k is the first-order rate constant. Methylene blue degradation experiments were repeated three times for each titania sample, and the calculated rate constants were within 5% error limit. A control experiment was also performed without using TiO_2 , which demonstrated almost no visible-light-induced decomposition of methylene blue in the absence of TiO_2 (Supporting Information, Figure S2).

3. RESULTS AND DISCUSSION

3.1. Formation of $\text{Ti}_{1-x}\text{S}_x\text{O}_{2-y}\text{N}_y$ Heterojunctions. The FT-IR spectra of control and thiourea-modified peroxo–titania xerogel samples were recorded (Figure 1) to investigate the

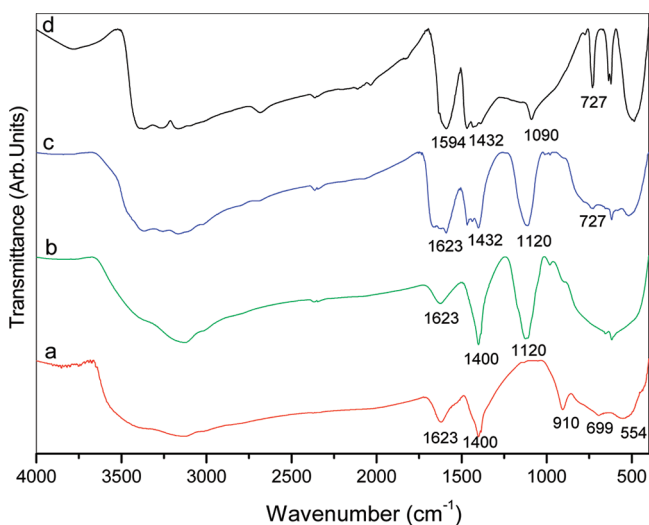


Figure 1. FT-IR spectra of 100 °C dried titania precursors: (a) control TiO_2 xerogel, (b) 0.1 TU- TiO_2 xerogel, (c) 0.8 TU- TiO_2 xerogel, and (d) thiourea.

effect of thiourea modification on the peroxo–titania complex structure. For the control and thiourea-modified peroxo–titania complexes, the stretching and bending vibrations of the OH group of adsorbed water molecules were observed as a broad peak between 3000 and 3600 cm^{-1} and a sharp peak at 1623 cm^{-1} .³⁸ The sharp peak at 1400 cm^{-1} was characteristic of N–H stretching vibrations of ammonia molecules from ammonia solution used for peroxo–titania complex synthesis.³⁹ For the control xerogel, the peaks corresponding to O–O and Ti–O–Ti bonds appeared at 910 and 554 cm^{-1} , respectively.^{38,40,41} On the other hand, the peaks characteristics of peroxo (O–O) bonds were not present in thiourea-modified peroxo–titania complexes. Thiourea has peaks corresponding to NH_2 scissoring, N–H stretching, C–N stretching, and C=S stretching at 1594, 1432, 1090, and 727 cm^{-1} .^{42–44} An increased C–N stretching frequency of 1120 cm^{-1} appeared in all thiourea-modified peroxo–titania complexes in comparison to the 1090 cm^{-1} for pure thiourea.⁴³ Identical C=S stretching frequency was observed for thiourea-modified peroxo–titania complexes and pure thiourea. Since both sulfur and nitrogen has the lone pair of electrons, thiourea can be coordinated to Ti^{4+} either through sulfur or nitrogen.⁴³ The absence of O–O bonds and the appearance of C–N stretching frequency at higher frequencies in thiourea-modified peroxo–titania complexes indicated the decomposition of peroxo–titania complex and coordination of thiourea to Ti^{4+} through nitrogen.⁴³ In addition, identical C=S stretching frequency observed for both pure thiourea and thiourea-modified peroxo–titania complexes also support the coordination of thiourea through nitrogen. Moreover, the orange color of peroxo–titania complex due to the presence of peroxo (O–O) bonds was not identified in thiourea-modified compositions, which also indicate the decomposition of the peroxo–titania complex. On the basis of these results and the fact that titania–peroxo complex exists as a binuclear complex (Supporting Information, Figure S3A),⁴⁵ a possible structure has been proposed for the Ti^{4+} –thiourea complex (Supporting Information, Figure S3B).

The low-temperature crystallization of anatase–rutile heterojunctions was identified from the X-ray diffraction (XRD) pattern of thiourea modified peroxo–titania complexes calcined

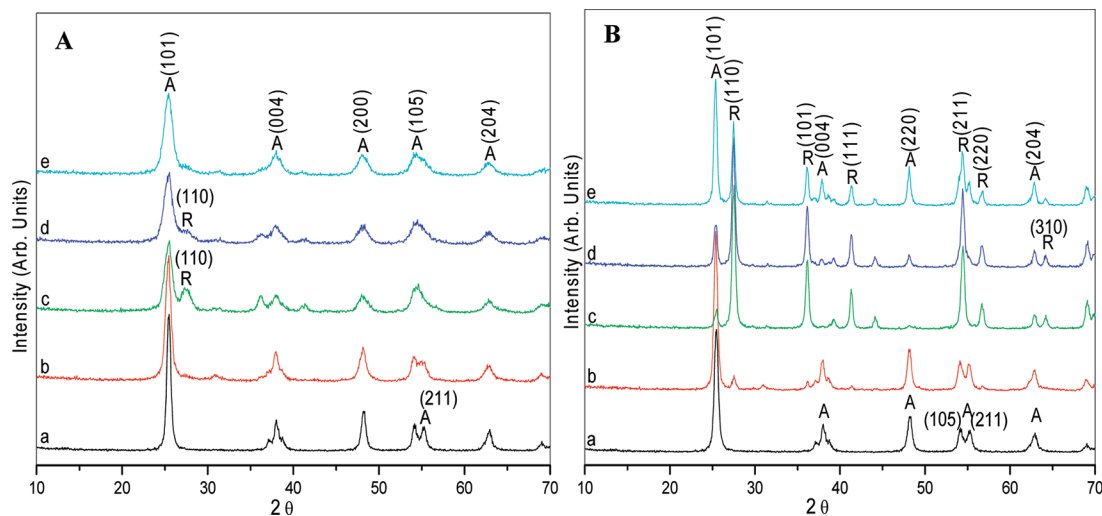


Figure 2. XRD of samples calcined at (A) 500 °C and (B) 700 °C: (a) control TiO_2 , (b) 0.1 TU- TiO_2 , (c) 0.2 TU- TiO_2 , (d) 0.4 TU- TiO_2 , and (e) 0.8 TU- TiO_2 (A = anatase; R = rutile).

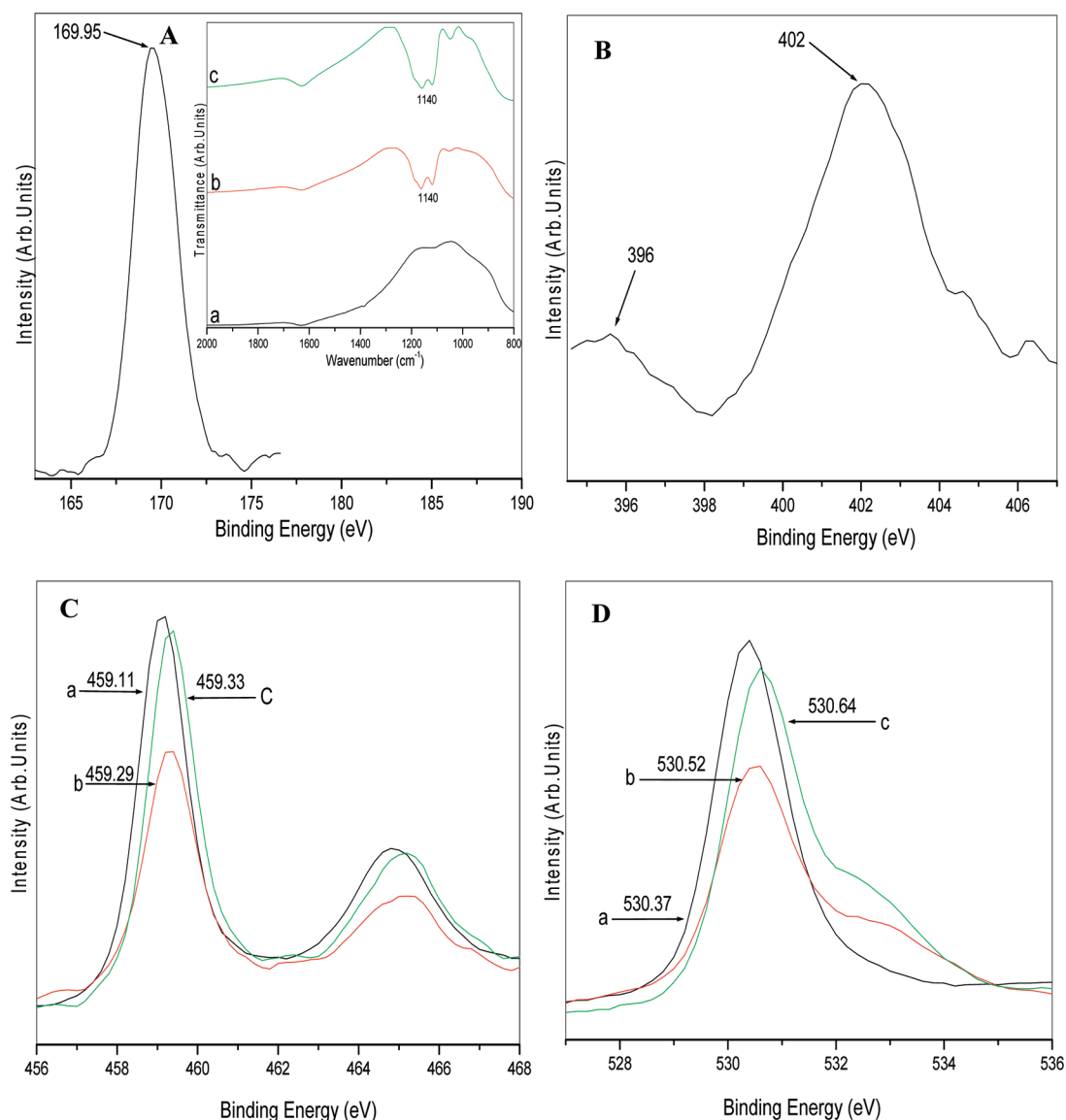


Figure 3. (A) S 2p XPS peaks of 0.8 TU-TiO₂ obtained at 600 °C. (Inset) FT-IR spectra of titania samples obtained at 600 °C: (a) control TiO₂, (b) 0.1 TU-TiO₂, and (c) 0.8 TU-TiO₂. (B) N 1s XPS peaks of 0.8 TU-TiO₂ obtained at 600 °C. (C) Ti 2p XPS peaks of titania calcined at 600 °C: (a) control TiO₂, (b) 0.1 TU-TiO₂, and (c) 0.8 TU-TiO₂. (D) O 1s XPS peaks of titania calcined at 600 °C: (a) control TiO₂, (b) 0.1 TU-TiO₂, and (c) 0.8 TU-TiO₂.

at various temperatures. The control titania exists as 100% anatase phase up to a calcination temperature of 800 °C (Figure 2B and Supporting Information, Figure S4B), whereas the thiourea-modified compositions 0.2 TU-TiO₂ and 0.4 TU-TiO₂ were converted to anatase–rutile mixtures at calcination temperatures of 500 and 600 °C (Figure 2A and Supporting Information, Figure S4A). At higher calcination temperatures of 700 and 800 °C, all thiourea-modified compositions exist as anatase–rutile mixtures. At all calcination temperatures, the highest amount of rutile phase was observed for 0.2 TU-TiO₂ (Supporting Information, Table S1). In addition to this, a gradual decrease in the crystallite size was identified with an increase of thiourea concentration (Supporting Information, Figure S5). The low-temperature crystallization of anatase–rutile heterojunctions was further confirmed by a more surface sensitive technique, Raman spectroscopy (Supporting Information, Figure S6).⁴⁶ The Raman-active modes for anatase ($A_{1g} + 2B_{1g} + 3E_g$ at 147, 197, 396, 515, and 638 cm⁻¹) and rutile (A_{1g}

+ $B_{1g} + B_{2g} + E_g$ at 144, 238, 447, and 611 cm⁻¹) were used as fingerprints.^{47–49} The low-temperature crystallization of anatase–rutile heterojunctions due to thiourea modification of peroxo–titania complexes can be explained by the structure of titania precursor. From our previous work, the in situ oxygen generation during the thermal decomposition of peroxo–titania complex was found to be responsible for the high-temperature anatase phase stability of control titania.² In the present case, peroxo–titania complex undergoes decomposition on reaction with thiourea and results in the formation of Ti⁴⁺–thiourea complex. This destabilization of the titania precursor due to peroxo (O–O) bond cleavage is believed to be responsible for the low-temperature crystallization S,N-codoped anatase–rutile heterojunctions. Increased anatase phase content and smaller crystallite size identified for compositions containing the higher amount of thiourea (0.4 TU-TiO₂ and 0.8 TU-TiO₂) can be attributed to the anatase stabilizing effect of sulfur and nitrogen.^{4,21}

Presence of sulfur and nitrogen in the heterojunctions was identified from the X-ray photoelectron spectroscopy (XPS) results. Sulfur present in the heterojunctions obtained at 600 °C has a characteristic S 2p_{3/2} peak at 169.95 eV (Figure 3A), which points toward the existence of S⁶⁺ cation of sulfate ions.^{25,50,51} This is in agreement with the triplet FT-IR peak centered at 1140 cm⁻¹ (Figure 3A inset), which indicates the fact that the sulfur exists as bidentate sulfate ions on the TiO₂ surface.^{21,50} It should be noted that the peaks characteristic of Ti–S bonds (162–163 eV) were not present in the S 2p spectra.⁵² This may be due to the fact that anionic doping is difficult to carry out because of the larger ionic radius of S²⁻ (1.7 Å) compared to that of O²⁻ (1.22 Å).⁵³ From the N 1s high-resolution spectra, it is clear that the heterojunctions obtained at 600 °C contain both interstitial (Ti–N–O at 402 eV) and lattice nitrogen (N–Ti–N at 396 eV) (Figure 3B).^{3,20,54} The low-intensity peaks observed at 404.5 and 406.5 represent surface-adsorbed nitrogen species such as NO_x and NH_x.^{55,56} Amount of sulfur and nitrogen present in the heterojunctions calcined at 500 and 600 °C are presented in Table 1. Regardless

Table 1. Amount of Sulfur and Nitrogen in Heterojunctions Calcined at 500 and 600 °C

composition	sulfur content (atom %)	nitrogen content (atom %)
0.1 TU-TiO ₂ obtained at 500 °C	3.31	0.91
0.2 TU-TiO ₂ obtained at 500 °C	3.51	1.13
0.4 TU-TiO ₂ obtained at 500 °C	3.84	1.25
0.8 TU-TiO ₂ obtained at 500 °C	4.12	1.38
0.1 TU-TiO ₂ obtained at 600 °C	3.08	0.67
0.2 TU-TiO ₂ obtained at 600 °C	3.15	0.85
0.4 TU-TiO ₂ obtained at 600 °C	3.48	0.96
0.8 TU-TiO ₂ obtained at 600 °C	3.90	1.02

of the fact that thiourea molecule contains S and N atoms in the ratio of 1:2, all S,N-codoped heterojunctions contain sulfur as the major dopant species. This can be related to the existence of sulfur as strongly coordinated sulfate ions in contrast to weakly bonded nitrogen-containing species. In addition to this, dopant concentrations were found to be increasing with an increase of thiourea concentration used for precursor modification, and the highest amount of S and N contents were present in 0.8 TU-TiO₂. This results from the formation of the higher amount of Ti⁴⁺–thiourea complexes and their thermal decomposition to anatase–rutile heterojunctions containing an increased amount of dopants. Reduced S and N content present in titania obtained at higher calcination temperature can be related to the evaporation of dopants at higher temperatures. All S,N-codoped heterojunctions have higher Ti 2p and O 1s binding energies compared to the control titania (Figure 3C,D). This can be attributed to the formation of bidentate complexes between titanium cation and sulfate anion, which strongly withdraws electrons from the neighboring Ti⁴⁺ ions resulting in an increase of Ti 2p and O 1s binding energies.⁵⁰ These increases in binding energies were consistent with the higher Ti–O–Ti

stretching frequencies identified from the FT-IR spectra of S,N-codoped heterojunctions (Supporting Information, Figure S7). Formation of an additional O 1s peak at 533.5 eV also suggested the presence of NO and NO₂ in the heterojunctions (Figure 3D).⁵⁷

Nanostructured S,N-codoped anatase–rutile heterojunctions have also been investigated by transmission electron microscopy (TEM). For instance, the average particle size of 0.2 TU-TiO₂ obtained at 600 °C was 12 ± 2 nm (Figure 4A,B), which

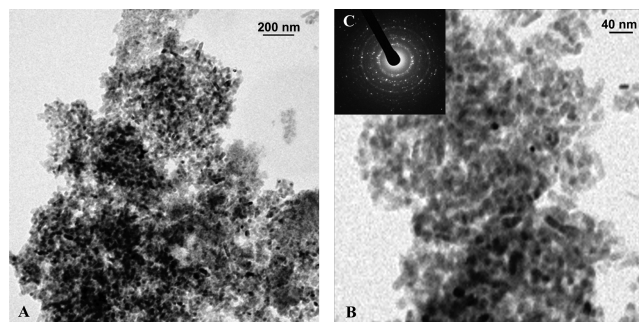


Figure 4. (A, B) Transmission electron micrograph and (C) SAED pattern of 0.2 TU-TiO₂ calcined at 600 °C.

was consistent with the average crystallite size obtained from the XRD analysis. The selected area electron diffraction (SAED) pattern recorded from 0.2 TU-TiO₂ obtained at 600 °C consists of a series of Debye–Scherrer rings (Figure 4C). The calculated *d*-spacing values of 3.38, 2.23, 1.70, and 1.22 Å represent the anatase lattice planes with Miller indices (101), (105), (004), and (204), respectively.^{58,59} Rutile lattice planes (110), (101), (111), and (220) were also identified from the corresponding *d*-spacing values of 2.90, 2.50, 2.10, and 1.59 Å.^{58,59} The complex SAED ring pattern of S,N-codoped heterojunctions confirmed the existence of polycrystalline anatase and rutile nanoparticles oriented in a random manner. Nitrogen adsorption isotherms of both control and S,N-codoped heterojunctions have type IV isotherms with H1 type of hysteresis (Supporting Information, Figure S8).⁶⁰ However, an increased steepness and ending of the hysteresis loop at a high relative pressure (*P*/*P*₀) of 0.7 with an increase of thiourea concentration is a measure of the high order of mesoporosity for S,N-codoped heterojunctions.⁶¹ Among the titania samples obtained at various calcination temperatures, S,N-codoped heterojunctions showed significantly higher surface area, pore size, and pore volume compared to the control sample (Table 2). Thus, it is evident from the above observations that the thiourea modification of the peroxo–titania complex results in the low-temperature crystallization of nanostructured S,N-codoped anatase–rutile heterojunctions possessing enhanced textural properties.

3.2. Electronic Structure of Heterojunctions. Optical absorption spectra of the control and S,N-codoped titania samples calcined at 600 °C are presented in Figure 5A. The control titania should be in general transparent in the visible region, whereas in the present case, control titania also absorb visible light. This can be related to the formation of oxygenated titania due to the thermal decomposition of peroxo–titania complex.² The in situ generation of oxygen results in the valence band widening and a consequent band gap narrowing of the control titania. In contrast to the control anatase titania, significant red shift in the absorption edge was identified for the

Table 2. Textural Properties of S,N-Codoped Heterojunctions Calcined at Various Temperatures

composition	surface area (m ² /g)	pore diameter (nm)	pore volume (cm ³ /g)
control TiO ₂ obtained at 500 °C	70.13	7.23	0.168
0.2 TU-TiO ₂ obtained at 500 °C	112.36	7.92	0.191
0.8 TU-TiO ₂ obtained at 500 °C	116.62	8.08	0.243
control TiO ₂ obtained at 600 °C	58.30	8.80	0.233
0.2 TU-TiO ₂ obtained at 600 °C	91.62	8.93	0.272
0.8 TU-TiO ₂ obtained at 600 °C	93.00	8.96	0.290
control TiO ₂ obtained at 700 °C	35.30	12.50	0.189
0.2 TU-TiO ₂ obtained at 700 °C	38.98	20.50	0.236
0.8 TU-TiO ₂ obtained at 700 °C	39.60	20.84	0.243
Degussa P-25	46.70	3.89	0.129

S,N-codoped samples. The band gap narrowing for S,N-codoped titania samples was directly proportional to the dopant concentration, and 0.8 TU-TiO₂ possesses the smallest band gap at all calcination temperatures (Table 3). In addition to this, band gap narrowing effects for these heterojunctions were more pronounced at higher calcination temperatures due to the additional contribution from the low band gap rutile phase. Similar red-shift in the absorption edge for S- and N-doped TiO₂ had been observed previously. For instance, Asahi et al. reported the band gap narrowing and enhanced visible-light photocatalytic activities of N-doped titania.^{20,54} On the basis of the density states calculations, they concluded that the N-atom substitutes for O in the anatase crystal and the band gap narrowing results from the mixing of N 2p states with O 2p states. Umebayashi et al. and Ohno et al. successfully synthesized anionic and cationic S-doped TiO₂, respectively, and explained the red-shift of the absorption edge by S 3p and O 2p mixing theory.^{22,26} However, recent theoretical studies attributed the band gap narrowing of S-doped TiO₂ to the S 3p states on the upper edge of the valence band.^{62,63} The local

Table 3. Band Gap Values of Heterojunctions Calcined at Various Temperatures

composition	band gap (eV)		
	500 °C	600 °C	800 °C
control TiO ₂	3.05	3.00	2.95
0.1 TU-TiO ₂	3.01	2.95	2.91
0.2 TU-TiO ₂	2.96	2.89	2.88
0.4 TU-TiO ₂	2.82	2.84	2.82
0.8 TU-TiO ₂	2.79	2.80	2.76

density approximation (LDA) calculations were conducted previously for the electronic structure analysis of S- and N-doped anatase TiO₂.^{64,65} These results revealed the fact that the band gaps of anion-doped TiO₂ are actually not narrowing, and the observed visible-light absorption results from the isolated impurity states located between the valence and conduction bands. Recent studies also suggested that lattice doping of anions is not necessary to induce band gap narrowing. For instance, the energy states created by substitutional nitrogen (N 2p) is positioned 0.14 eV above the valence band, whereas interstitial nitrogen (π* N–O) states lie higher in the gap at 0.73 eV.^{32,64,65} It is also reported that cationic S-doping creates an additional S 3p level positioned 0.38 eV above the valence band of TiO₂.⁶³

As identified from the FT-IR and XPS studies, the S,N-codoped TiO₂ contains surface-adsorbed sulfate ions and lattice and interstitial nitrogen as dopant species. In order to demonstrate the effect of S and N impurities on the electronic structure of titania, valence band (VB) XPS were performed. Since anatase and rutile phase titania has different band gap values and electronic structure, pure anatase titania and 0.8 TU-TiO₂ calcined at 600 °C were selected for comparison. Identical VB maximum of 1.95 eV were identified from the XPS spectra of these samples (Figure 5B), which was in agreement with the previous reports for pure anatase phase titania.^{2,66,67} Moreover, the equal width of their VB of 9.5 eV represents almost similar mobilities of the photogenerated charge carriers. These results rule out the possibility of N 2p and S 3p mixing with O 2p bands and a consequent band gap narrowing. It should also be noted that the electronegativity of dopant atoms extensively determines the nature of doping. As a result of the low

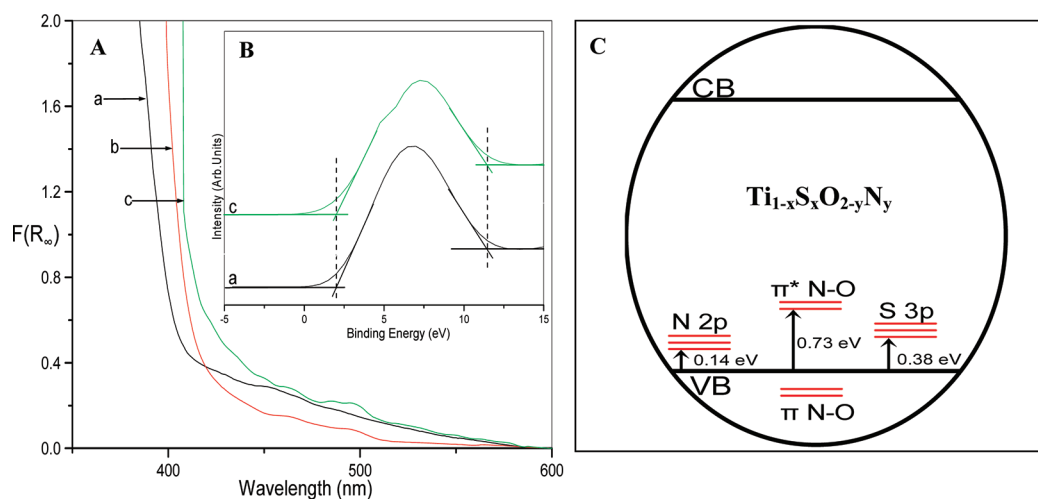


Figure 5. (A) UV-vis absorption spectra and (B) valence band XPS spectra of titania samples calcined at 600 °C: (a) control TiO₂, (b) 0.2 TU-TiO₂, and (c) 0.8 TU-TiO₂. (C) Electronic structure of Ti_{1-x}S_xO_{2-y}N_y.

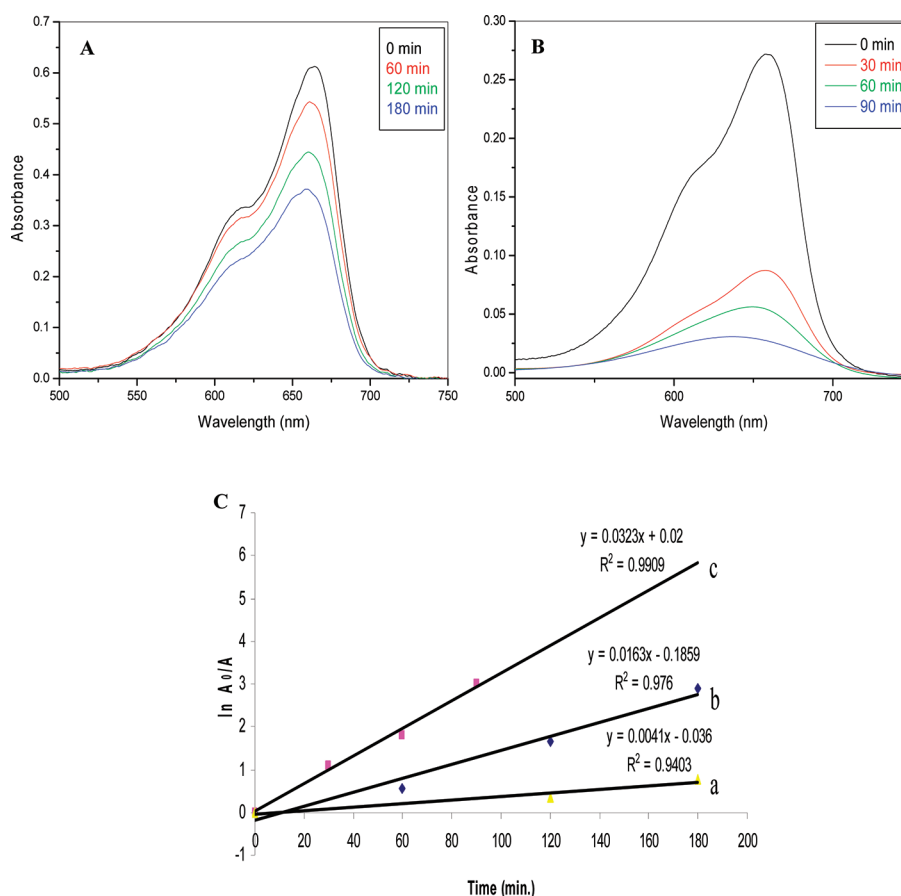


Figure 6. Absorption spectra of visible-light induced methylene blue degradation using (A) Degussa P-25 and (B) 0.2 TU-TiO₂ calcined at 600 °C. (C) Kinetic study of (a) Degussa P-25, (b) control TiO₂ calcined at 600 °C, and (c) 0.2 TU-TiO₂ calcined at 600 °C.

electronegativity of S and N atoms (2.58 and 3.04, respectively) in comparison to oxygen (3.44), only low mixing of S 3p and N 2p bands with O 2p bands can be expected for S- and N-doped TiO₂.^{64,65} Therefore, the band gap narrowing for the S,N-codoped titania can be explained by the isolated S 3p, N 2p, and Π^* N–O states in the band gap rather than the N 2p and S 3p mixing with O 2p bands (Figure 5C).

3.3. Visible-Light-Induced Photocatalytic Activity of Heterojunctions. S,N-Codoped anatase–rutile heterojunctions obtained at various calcination temperatures exhibited enhanced visible-light-induced photocatalytic activities in comparison to the control titania (Supporting Information, Table S2). In the case of heterojunctions calcined at 500 and 600 °C, 0.2 TU-TiO₂ containing 29% and 38% of rutile phase, respectively, exhibited the highest photocatalytic activity. At the higher calcination temperatures of 700 and 800 °C, 0.2 TU-TiO₂ has converted to 88% and 96% of less photoactive rutile phase. As a result, 0.8 TU-TiO₂ containing the highest amount of S and N was the most photoactive sample. The most active S,N-codoped heterojunction 0.2 TU-TiO₂ obtained at 600 °C containing 62% anatase and 38% rutile exhibited 2-fold and 8-fold higher visible-light photocatalytic activities compared to the control titania (100% anatase) and the standard photocatalyst Degussa P-25 (70% anatase + 30% rutile), respectively (Figure 6C). The calculated rate constants for 0.2 TU-TiO₂ obtained at 600 °C, control titania calcined at 600 °C, and Degussa P-25 were 0.0323, 0.0163, and 0.004 min^{−1}, respectively. In addition, higher blue-shifts for methylene blue absorption peaks were also identified during the photocatalytic

experiment of heterojunction samples in contrast to the control sample (Figure 6A,B), which indicates faster dye degradation through the N-demethylation mechanism.^{36,37} The visible-light-induced photocatalytic activity of the control TiO₂ prepared through the peroxo–titania route can be related to its visible-light absorption due to oxygen excess defects.²

Significantly higher visible-light photocatalytic activities of S,N-codoped heterojunctions can be explained by the gap narrowing, efficient anatase to rutile charge transfer, and nanocrystalline nature. It is clear from the XRD, FT-IR, XPS and UV–vis spectroscopy results that the heat treatment of thiourea-modified peroxo–titania complex results in the formation of visible-light active S,N-codoped anatase–rutile heterojunctions. Recent studies suggested that both interstitial and lattice anion doping can cause band gap narrowing and enhanced visible-light photocatalytic activities.^{32,64,65} In the present study, the additional energy levels due to sulfate ions and lattice and interstitial nitrogen impurities result in an effective band gap narrowing and increased visible-light photocatalytic activities. In addition to this, an increase in the surface acidity of TiO₂ due to the electron-withdrawing inductive effect of sulfate ions on the metallic cation also result in an enhancement of photocatalytic activity.⁶⁸ Thus, the overall increase of photocatalytic activities observed on increasing the thiourea concentration results from an increased band gap narrowing due to the higher dopant concentration. The partial removal of dopants at higher calcination temperatures may be responsible for the reduced photocatalytic activities of high-temperature calcined samples (for example, at

700 and 800 °C). Improved textural properties of S,N-codoped anatase–rutile heterojunctions may be another factor responsible for their superior photocatalytic activities. Photocatalytic activities are known to be greatly affected by the surface area of the catalysts. It is clear that all S,N-codoped titania samples calcined at 500 and 600 °C possess superior surface area, pore diameter, and pore volume in contrast to the control titania and the standard photocatalyst Degussa P-25 (Table 2). As a result, these heterojunctions can adsorb and decompose a higher amount of methylene blue. For example, the most active heterojunction 0.2 TU-TiO₂ obtained at 600 °C, which has a surface area of 91.62 m²/g, adsorbs more MB than the standard photocatalyst Degussa P-25 with a surface area of 46.70 m²/g (Supporting Information, Figure S9). Thus, it can be concluded that the improved textural properties of S,N-codoped TiO₂ heterojunctions is an important factor responsible for their enhanced photocatalytic activities.

Since the S,N-codoped titania heterojunctions possess enhanced textural properties, reduced band gap, and a variety of anatase/rutile ratios, it is necessary to differentiate the critical factor responsible for the enhanced visible-light photocatalytic activity. In order to find this, the visible-light photocatalytic activity of the most active anatase–rutile heterojunction 0.2 TU-TiO₂ obtained at 600 °C (which has a surface area of 91.62 m²/g and band gap of 2.89 eV) was compared with that of anatase phase 0.8 TU-TiO₂ obtained at 500 °C (which has a surface area of 116.62 m²/g and band gap of 2.79 eV). The calculated photocatalytic rate constants for methylene blue degradation clearly showed the fact that the single-phase photocatalyst exhibits lower photocatalytic activity (Supporting Information, Table S2) despite its better textural properties and increased visible-light absorption. These results proved the fact that the coexistence of anatase and rutile phase is the critical factor responsible for the superior visible-light-induced photocatalytic activities of S,N-codoped heterojunctions. On the other hand, for a series of titania heterojunctions containing optimum rutile content, enhanced textural properties and increased visible-light absorption may act as secondary factors for increasing the photocatalytic activity.

In order to further confirm the fact that the presence of low band gap rutile phase is the critical factor responsible for the enhanced photocatalytic activities of S,N-codoped heterojunctions, single phase and heterojunction titania samples were subjected to photoluminescence (PL) spectroscopy. Since the PL emission results from the recombination of photo-induced charge carriers, information regarding the presence of surface states, the efficiency of charge carrier trapping, and their recombination kinetics can be drawn from the PL spectra. This technique has been widely used in order to understand the fate of electron–hole pairs in semiconductor particles, and a strong correlation between PL intensity and photocatalytic activity has been previously reported.^{2,3,69} The observed PL spectra can be attributed to the radiative recombination process (Figure 7). Much higher band–band and excitonic PL intensities were identified for pure anatase, pure rutile, and 0.8 TU-TiO₂ obtained at 500 °C (100% anatase), in contrast to the photocatalytically most active S,N-codoped heterojunction 0.2 TU-TiO₂ obtained at 600 °C (62% anatase + 38% rutile) and Degussa P-25 (70% anatase + 30% rutile). This indicates the fact that the coexistence of anatase and rutile phase is responsible for the poor PL intensities of 0.2 TU-TiO₂ and Degussa P-25.

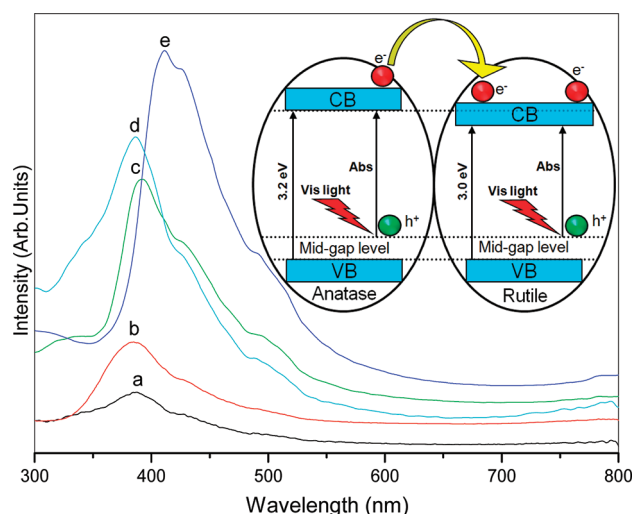


Figure 7. Photoluminescence spectra of (a) 0.2 TU-TiO₂ calcined at 600 °C, (b) Degussa P-25, (c) 0.8 TU-TiO₂ calcined at 500 °C, (d) pure anatase, and (e) pure rutile. (Inset) Electron transfer mechanism in Ti_{1-x}S_xO_{2-y}N_y anatase–rutile heterojunctions.

It is well-established that the phase composition plays an important role in the PL intensities and photocatalytic activities of titania.^{3,14,34,70} The phenomenon of photocatalysis involves a competitive formation of electron–hole pairs and their recombination. Any factor reducing the electron–hole recombination rate can reduce the PL intensity, which results in an increase of the photocatalytic activities. Enhanced photocatalytic activities of anatase–rutile heterojunctions related to lower PL intensities were also reported in the literature.³ The photocatalytically most active heterojunction 0.2 TU-TiO₂ obtained at 600 °C consists of 62% anatase and 38% rutile, both possessing an average particle size of 12 ± 2 nm (Figure 4). The conduction band of rutile phase is 0.2 eV lower than that of the anatase phase; as a result, the photoexcited electrons (from the mid gap level) can be effectively transferred from the conduction band of S,N-codoped anatase to the conduction band of rutile (Figure 7, inset).^{3,14,34} This electron–hole separation effect slows down the photoexcited charge carrier recombination and results in an increase of photocatalytic activity. In addition to this, photoexcited electrons formed on rutile can be transferred to the defect states of anatase. It is therefore proposed that the efficient electron–hole separation due to anatase to rutile electron transfer is responsible for the superior visible-light-induced photocatalytic activities of S,N-codoped TiO₂ heterojunctions.

4. CONCLUSIONS

Highly visible-light-active S,N-codoped anatase–rutile heterojunctions were developed through a thiourea modified peroxo–titania route. The FT-IR studies point toward the formation of a Ti⁴⁺–thiourea complex as a result of thiourea modification of the peroxo–titania complex. The existence of sulfur as sulfate ions (S⁶⁺) and nitrogen as lattice (N–Ti–N) and interstitial (Ti–N–O) species in heterojunctions was confirmed using X-ray photoelectron spectroscopy and FT-IR spectroscopic techniques. Formation of isolated S 3p, N 2p, and Π^* N–O states between the valence and conduction bands was found to be responsible for the band gap narrowing of S,N-codoped titania. In addition to this, S,N-codoped heterojunctions

possesses smaller crystallite sizes and improved textural properties compared to the undoped titania. The most active S,N-codoped heterojunction 0.2 TU-TiO₂ obtained at 600 °C containing 62% anatase and 38% rutile showed 2- and 8-fold higher visible-light photocatalytic activities in comparison to the control titania and the standard photocatalyst Degussa P-25, respectively. Efficient electron–hole separation due to anatase to rutile electron transfer was identified as the critical factor responsible for the superior visible-light-induced photocatalytic activities of S,N-codoped anatase–rutile heterojunctions. These S,N-codoped anatase–rutile heterojunctions can be effectively employed for visible-light-induced photocatalytic, photovoltaic, and self-cleaning antibacterial applications.

■ ASSOCIATED CONTENT

■ Supporting Information

Additional experimental details, transmission spectrum of primary blue filter used for photocatalytic study, methylene blue degradation in the absence of TiO₂, structure of TiO₂ precursors, XRD patterns of titania calcined at 600 and 800 °C, effect of thiourea concentration on TiO₂ crystallite size, Raman spectra of titania calcined at 500 and 600 °C, FT-IR spectra of calcined titania, N₂ adsorption–desorption isotherm of titania calcined at 600 °C, absorption spectra of methylene blue at regular time intervals in the absence of visible light, anatase and rutile content present in S,N-codoped titania calcined at various temperatures, and photocatalytic rate constants of S,N-codoped titania. This material is available free of charge via the Internet at <http://pubs.acs.org/>.

■ AUTHOR INFORMATION

Corresponding Author

*E-mail: suresh.pillai@dit.ie.

Notes

The authors declare no competing financial interest.

■ ACKNOWLEDGMENTS

The authors would like to thank Enterprise Ireland for funding (CFTD/06/IT/326 and ARE/2008/0005) and Dr. John Colreavy (Director, Centre for Research in Engineering Surface Technology) for supporting this study and for providing valuable suggestions.

■ REFERENCES

- (1) O'Regan, B.; Grätzel, M. *Nature* **1991**, 353, 737.
- (2) Etacheri, V.; Seery, M. K.; Hinder, S. J.; Pillai, S. C. *Adv. Funct. Mater.* **2011**, 21, 3744.
- (3) Etacheri, V.; Seery, M. K.; Hinder, S. J.; Pillai, S. C. *Chem. Mater.* **2010**, 22, 3843.
- (4) Pillai, S. C.; Periyat, P.; George, R.; McCormack, D. E.; Seery, M. K.; Hayden, H.; Colreavy, J.; Corr, D.; Hinder, S. J. *J. Phys. Chem. C* **2007**, 111, 1605.
- (5) Mills, A.; Lee, S. K. *J. Photochem. Photobiol., A* **2002**, 152, 233.
- (6) Kamat, P. V. *J. Phys. Chem. C* **2007**, 111, 2834.
- (7) Yuan, J.; Tsujikawa, S. *J. Electrochem. Soc.* **1995**, 142, 3444.
- (8) Honda, H.; Ishizaki, A.; Soma, R.; Hashimoto, K.; Fujishima, A. *J. Illum. Eng. Soc.* **1998**, 42, 27.
- (9) Ollis, D. F.; Al-Ekabi, H. *Photocatalytic Purification and Treatment of Water and Air*; Elsevier: Amsterdam, 1993.
- (10) Grinis, L.; Kotlyar, S.; Ruhle, S.; Grinblat, J.; Zaban, A. *Adv. Funct. Mater.* **2010**, 20, 282.
- (11) Pugh, S. L.; Guthrie, J. T. *Dyes Pigm.* **2002**, 55, 109.
- (12) Cai, R.; Kubota, Y.; Shuin, T.; Sakai, H.; Hashimoto, K.; Fujishima, A. *Cancer Res.* **1992**, 52, 2346.
- (13) Choi, W.; Termin, A.; Hoffmann, M. R. *J. Phys. Chem.* **1994**, 98, 13669.
- (14) Kavan, L.; Grätzel, M.; Gilbert, S. E.; Klemen, C.; Scheel, H. J. *J. Am. Chem. Soc.* **1996**, 118, 6716.
- (15) Beyers, E.; Cool, P.; Vansant, E. F. *J. Phys. Chem. B* **2005**, 109, 10081.
- (16) Linsebigler, A. L.; Lu, G.; Yates, Y. T. *Chem. Rev.* **1995**, 95, 735.
- (17) Fox, M. A.; Dulay, M. T. *Chem. Rev.* **1993**, 93, 341.
- (18) Muruganandham, M.; Swaminathan, M. *Sol. Energy Mater. Sol. Cells* **2004**, 81, 439.
- (19) Miyagi, T.; Kamei, M.; Mitsuhashi, T.; Ishigaki, T.; Yamazaki, A. *Chem. Phys. Lett.* **2004**, 390, 399.
- (20) Asahi, R.; Morikawa, T.; Ohwaki, T.; Aoki, K.; Taga, Y. *Science* **2001**, 293, 269.
- (21) Periyat, P.; McCormack, D. E.; Hinder, S. J.; Pillai, S. C. *J. Phys. Chem. C* **2009**, 113, 3246.
- (22) Umabayashi, T.; Yamaki, T.; Itoh, H.; Asai, K. *Appl. Phys. Lett.* **2002**, 81, 454.
- (23) Umabayashi, T.; Yamaki, T.; Tanaka, S.; Asai, K. *Chem. Lett.* **2003**, 32, 330.
- (24) Ohno, T.; Mitsui, T.; Matsumura, M. *Chem. Lett.* **2003**, 32, 364.
- (25) Ohno, T.; Akiyoshi, M.; Umabayashi, T.; Asai, K.; Mitsui, T.; Matsumura, M. *Appl. Catal. A: Gen.* **2004**, 265, 115.
- (26) Ohno, T. *Water Sci. Technol.* **2004**, 49, 159.
- (27) Takeshita, K.; Yamakata, A.; Ishibashi, T.; Onishi, H.; Nishijima, K.; Ohno, T. *J. Photochem. Photobiol. A: Chem.* **2006**, 177, 269.
- (28) Rengifo-Herrera, J. A.; Pulgarin, C. *Sol. Energy* **2010**, 84, 37.
- (29) Xu, J.-H.; Li, J.; Dai, W.-L.; Cao, Y.; Li, H.; Fan, K. *Appl. Catal. B: Environ.* **2008**, 79, 72.
- (30) Rengifo-Herrera, J. A.; Mielczarski, E.; Mielczarski, J.; Castillo, N. C.; Kiwi, J. *Appl. Catal. B: Environ.* **2008**, 84, 448.
- (31) Torres, G. R.; Lindgren, T.; Lu, J.; Granqvist, C.-G.; Lindqvist, S.-E. *J. Phys. Chem. B* **2004**, 108, 5995.
- (32) Valentin, C. D.; Pacchioni, G.; Selloni, A.; Livraghi, S.; Giamello, E. *J. Phys. Chem. B* **2005**, 109, 11414.
- (33) Junin, C.; Thanachayanont, C.; Euvananont, C.; Inpor, K.; Limthongkul, P. *Eur. J. Inorg. Chem.* **2008**, 2008, 974.
- (34) Kawahara, T.; Konishi, Y.; Tada, H.; Tohge, N.; Nishii, J.; Ito, S. *Angew. Chem., Int. Ed.* **2002**, 41, 2811.
- (35) Hamal, D. B.; Klabunde, K. J. *J. Colloid Interface Sci.* **2007**, 311, 514.
- (36) Zhang, Y.; Xu, H.; Xu, Y.; Zhang, H.; Wang, Y. *J. Photochem. Photobiol. A: Chem.* **2005**, 170, 279.
- (37) Yu, J. R.; Hoi, W. C. *Environ. Sci. Technol.* **2008**, 42, 294.
- (38) Karuppachamy, S.; Jeong, J. M. *J. Oleo Sci.* **2006**, 55, 263.
- (39) Rhee, C. H.; Lee, J. S.; Chung, S. H. *J. Mater. Res.* **2005**, 20, 3011.
- (40) Yoko, T.; Kamiya, K.; Tanaka, K. *J. Mater. Sci.* **1990**, 25, 3922.
- (41) Ayers, M. R.; Hunt, A. J. *Mater. Lett.* **1998**, 34, 290.
- (42) Selvasekarapandian, S.; Vivekanandan, K.; Kolandaivel, P.; Gundurao, T. K. *Cryst. Res. Technol.* **1997**, 32, 299.
- (43) Anie, R.; Joseph, C.; Ittyachen, M. A. *Mater. Lett.* **2001**, 49, 299.
- (44) Stewart, J. E. *J. Chem. Phys.* **1957**, 26, 248.
- (45) Schwarzenbach, D. *Inorg. Chem.* **1970**, 9, 2391.
- (46) Gao, K. *Physica B* **2007**, 398, 33.
- (47) Ohsaka, T.; Izumi, F.; Fujiki, Y. *J. Raman Spectrosc.* **1978**, 7, 321.
- (48) Berger, H.; Tang, H.; Lévy, F. *J. Cryst. Growth* **1993**, 130, 108.
- (49) Tang, H.; Prasad, K.; Sanjines, R.; Schmid, P. E.; Levy, F. *J. Appl. Phys.* **1994**, 75, 2042.
- (50) Mao, W.; Ma, H.; Wang, B. *J. Hazard. Mater.* **2009**, 167, 707.
- (51) Colon, G.; Hidalgo, M. C.; Munuera, G.; Ferino, I.; Cutrufello, M. G.; Navio, J. A. *Appl. Catal. B: Environ.* **2006**, 63, 45.
- (52) Ho, W.; C.Yu, J.; Lee, S. J. *Solid State Chem.* **2006**, 179, 1171.
- (53) Dong, F.; Zhao, W.; Wu, Z. *Nanotechnology* **2008**, 19, 365607.
- (54) Morikawa, T.; Asahi, R.; Ohwaki, T.; Aoki, K.; Taga, Y. *Jpn. J. Appl. Phys.* **2001**, 40, L561.
- (55) Mrowetz, M.; Balcerski, W.; Colussi, J.; Hoffmann, M. R. *J. Phys. Chem. B* **2004**, 108, 17269.

- (56) Gole, J. L.; Stout, J. D.; Burda, C.; Lou, Y.; Chen, X. J. *Phys. Chem. B* **2004**, *108*, 1230.
- (57) Rodriguez, J. A.; Jirsak, T.; Dvorak, J.; Sambasivan, S.; Fischer, D. J. *Phys. Chem. B* **2000**, *104*, 319.
- (58) Miao, L.; Jin, P.; Kaneko, K.; Terai, A.; Nabatova-Gabain, N.; Tanemura, S. *Appl. Surf. Sci.* **2003**, *212*, 255.
- (59) Miao, L.; Tanemura, S.; Kondo, Y.; Iwata, M.; Toh, S.; Kaneko, K. *Appl. Surf. Sci.* **2004**, *238*, 125.
- (60) Nasar, R. S.; Cerqueira, M.; Longo, E.; Varela, J. A. *Cerâmica* **2008**, *54*, 38.
- (61) Kartini, I.; Meredith, P.; Costa, J. C. D. D.; Lu, G. Q. *J. Sol–Gel Sci. Technol.* **2004**, *31*, 185.
- (62) Cui, Y.; Du, H.; Wen, L. *Solid State Commun.* **2009**, *149*, 634.
- (63) Tian, F.; Liu, C.; Zhao, W.; Wang, X.; Wang, Z.; Yu, J. C. *J. Comput. Sci. Eng.* **2011**, *1*, 32.
- (64) Tian-hua, X.; Chen-lu, S.; Yong, L.; Gao-rong, H. *J. Zhejiang Univ. Sci. B.* **2006**, *7*, 299.
- (65) Segall, M. D.; Lindan, P. J. D.; Probert, M. J.; Pickard, C. J.; Hasnip, P. J.; Clark, S. J.; Payne, M. C. *J. Phys.: Condens. Matter* **2002**, *14*, 2717.
- (66) Pan, J.; Liu, G.; Lu, G. Q.; Cheng, H. M. *Angew. Chem., Int. Ed.* **2011**, *50*, 2133.
- (67) Zheng, G.; Wang, J.; Liu, X.; Yang, A.; Song, H.; Guo, Y.; Wei, H.; Jiao, C.; Yang, S.; Zhu, Q.; Wang, Z. *Appl. Surf. Sci.* **2010**, *256*, 7327.
- (68) Noda, L. K.; Almeida, R. M. d.; Probst, L. F. D.; Goncalves, N. S. *J. Mol. Catal. A: Chem.* **2005**, *225*, 39.
- (69) Liqiang, J.; Yichun, Q.; Baiqi, W.; Shudan, L.; Baojiang, J.; Libin, Y.; Wei, F.; Honggang, F.; Jiazhong, S. *Sol. Energy Mater. Sol. Cells* **2006**, *90*, 1773.
- (70) Balasubramanian, G.; Dionysiou, D. D.; Suidan, M. T.; Baudin, I.; Laine, J. M. *Appl. Catal., B* **2004**, *47*, 73.